Materials Research Bulletin 120 (2019) 110585

Contents lists available at ScienceDirect

Materials Research Bulletin

journal homepage: www.elsevier.com/locate/matresbu

Influence of thermal annealing on the properties of evaporated Er-doped SnO_2

Diego H.O. Machado, José H.D. da Silva, Américo Tabata, Luis V.A. Scalvi*

UNESP, São Paulo State University, Department of Physics, FC and Graduate Program in Materials Science and Technology (POSMAT), Bauru, SP, Brazil

ARTICLE INFO

Keywords:
Tin dioxide
Resistive evaporation
Sol-gel
Erbium
Thin films

ABSTRACT

Er-doped tin dioxide thin films, deposited on glass substrates by a combination of sol-gel and resistive evaporation techniques, are investigated. The sol-gel route is used for powder preparation, which serves as material source for resistively evaporated thin films. The annealing temperature influences the Er^{3+} location, that reflects on the photoluminescence (PL) related to $^2H_{11/2} \rightarrow {}^4I_{15/2}$ and $^4S_{3/2} \rightarrow {}^4I_{15/2}$ Er^{3+} transitions. The lower annealing temperature, 300 °C, leads to PL emission, which vanishes for higher annealing temperatures. Annealing temperature above 300 °C enlarges the crystallites and allows diffusion of Er ions into the sample, increasing the population of substituted Sn sites. Then, the population of grain boundary located luminescent sites is decreased, leading to higher conductivity concomitant with absence of PL signal. Evaporated SnO_2 films have the advantage of a stable electrical signal and the deposition on hydrophobic surfaces. Emission of evaporated SnO_2 on GaAs substrates is also shown, yielding the substrate influence.

1. Introduction

Tin oxide (SnO_2) presents naturally *n-type* conduction due to oxygen vacancies and interstitial tin atoms [1–4]. It has wide bandgap (3.6–4.0 eV), and the conductivity usually depends on the deposition method [1–3], being moderate in the case of sol-gel routes, since the grains are rather small [5], influencing the electron scattering. When deposited by evaporation techniques the conductivity has similar magnitudes of sol-gel routes [5,6], although, evaporated SnO_2 films have a more stable electrical signal when compared to films deposited by sol-gel-dip-coating. In addition, the evaporation technique allows SnO_2 to be deposited on hydrophobic surfaces, which may become an obstacle when the oxide film is deposited by chemical routes [7,8]. Further, the use of evaporation techniques allows for the use of shadow masks, in order to achieve the desired sample/film design.

SnO_2 usually crystallizes in the tetragonal rutile structure [2,4,9–12] and presents transparency above 90% in the visible region [2,10,11,13], properties that enable the use of SnO_2 for applications in transparent conducting electrodes [14–16] liquid crystal and optoelectronic devices [14,17–19], heat mirrors and solar energy conversion devices [16,20]. Other applications can be found, such as gas sensor [1,3,4,15,17,20–22], solar cells [16,20], lithium ion batteries [20], photo catalysis [17,21,23] and supercapacitors [17,24]. Thin films of this semiconductor oxide can be deposited by different methods such as magnetron sputtering [2,4,10,11,25], dip and spin coating by sol-gel processes [1,5,7,19,26–29], chemical vapor deposition (CVD) [2,4,13,22], spray pyrolysis [4,22], pulsed laser deposition [16], chemical bath deposition (CBD) [1] and resistive evaporation [4,6,22].

Nowadays there is ample interest in the study of new materials prepared by the sol-gel route, which presents some advantages when compared to other techniques, such as the facility of deposition in complex forms, easy doping control and relative simple equipment [26,27,30]. Although in this work resistive evaporation is preferred to chemical routes for thin film deposition, the sol-gel solution is the precursor for synthesizing the SnO_2 powder used in the evaporation. Many kinds of dopants have been studied to improve the optical and electrical properties of different devices applications [2,4,13,26,31]. Concerning rare-earth doping, the threefold oxidation state (RE^{3+}) exhibits luminescence due to 4f core transitions, which are practically independent of the host matrix. In the case of Er^{3+}, these transitions yield several emission lines from visible to infrared. In particular, the transition at about 1540 nm coincides with the minimum optical absorption from silica based optical fibers [32,33], and is suitable for use in optical amplifiers. Er^{3+}-doped materials are suitable in up-conversion processes due to the Er^{3+} energy level configuration. Different mechanisms explain the up-conversion, and among them, the most efficient is an excited state absorption (ESA) of individual Er^{3+} ions or the energy transfer involving two ions [26].

* Corresponding author.
E-mail address: luis.scalvi@unesp.br (L.V.A. Scalvi).

https://doi.org/10.1016/j.materresbull.2019.110585
Received 4 January 2019; Received in revised form 8 August 2019; Accepted 13 August 2019
Available online 14 August 2019
0025-5408/ © 2019 Elsevier Ltd. All rights reserved.

The incorporation of Er^{3+} into the SnO_2 matrix increases the resistivity of the naturally n-type material when compared to films without doping, because Er^{3+} ions replace Sn^{4+} in the SnO_2 matrix, leading to charge compensation with free electrons, since the Er^{3+} ions act as acceptors. Another effect that occurs in the incorporation of trivalent rare earth ions is an increase in the density per unit area of intergranular potential barriers, since the doping decreases the size of the crystallites, increasing the concentration of crystallites, causing the decrease of the electronic mobility in the material [34]. The Er^{3+} transitions in the electromagnetic spectrum [26,19,35] are very suitable for several optoelectronic applications, such as displays [36], amplifiers and lasers [19,37], among others [19,34–38]. Usually Er-doped SnO€$_2$ can also be used in optical amplifiers and electroluminescent devices where electron-hole energy is transferred to Er^{3+} ion [36,37].

In this work, Er^{3+}-doped tin dioxide thin films produced through a combination of sol-gel and evaporation route are investigated. In this new route the sol-gel method is used for the powder preparation, including the doping, and then the thin film is deposited by resistive evaporation on different substrates. The role of the annealing temperature for the morphological, optical and electrical properties, and the influence of distinct substrates, are reported. The success of this new route for the SnO_2 preparation is related to the visible light emission from the samples in the form of thin films, a very suitable format for integration in optoelectronic devices, along with simple electro-optical excitation of Er^{3+} ion.

2. Experimental

2.1. Synthesis of thin film samples

Preparation of sol-gel tin dioxide (SnO_2) solution was carried out by using $ErCl_3$ added to SnO_2 solution to form SnO_2:1at%Er^{3+}. The Er-doped SnO_2 powder was previously obtained by evaporation of solvent in the sol-gel solution, and then, used in the resistive evaporation. The deposition was carried out in a self-purpose built system having a resistive molybdenum crucible as the evaporation vessel. Films were deposited on soda-lime glass, quartz and GaAs substrates, as described in Table 1. The residual pressure in the chamber was about 10^{-5} torr. The deposited samples were thermally annealed at 300 °C, 500 °C and 1000 °C, as also described in Table 1, which summarizers the given labels and the conditions for obtaining the SnO_2 samples deposited by resistive evaporation on different substrates.

2.2. Characterization

X-ray diffraction (XRD) analysis was performed by using a MiniFlex 600/RIGAKU in the 20-80° range in the powder mode. Metal contacts of in were also deposited by resistive evaporation in a Edwards evaporation system model auto 500. Scanning electron microscopy (SEM) and X-ray dispersive energy (EDX) measurements were performed on a scanning electron microscope of Carl Zeiss model LS15. Atomic Force microscopy (AFM) measurements were performed on a Park Systems, model XE7, which was operated in contact mode using CONTSCR 10 M tips. Photoluminescence (PL) measurements were carried out using excitation by a He-Cd laser (325 nm) and the signal was detected by a GaAs photomultiplier detector. In these measurements, the sample temperature was controlled by using a He-closed cycle Janis cryostat.

For voltage dependent current measurements (IxV) at different temperatures, the samples were placed in a cryostat of He-closed cycle APD - Cryogenics compressor. The resistivity data were calculated from the measured IxV curves. Measurements were performed in the dark and under the irradiation effect of different light sources: 1) He-Ne laser (628 nm) and 2) InGaN LEDs (440–460 nm), and 3) He-Cd laser (325 nm). The first light source has energy far below the SnO_2 bandgap, whereas the second one has energy closer to it but still below the bandgap, and the former has energy above the SnO_2 fundamental absorption edge. Electrical characterization measurements were performed by using a Keithley 2400-C source meter.

Table 1
Samples used in this work, deposited on different types of substrate, and submitted to distinct thermal annealing.

Sample Name	Substrate	Annealing temperature/time
S1000	Quartz	1000 °C/1hour
S500	Soda lime	500 °C/5hours
S300		300 °C/5hours
S0		as deposited
GS1	GaAs	as deposited
GS2		as deposited

3. Results and discussion

3.1. Structural and morphological characterization

X-ray diffraction patterns of SnO_2 films doped with 1at% Er^{3+}, with different thermal treatments, are presented in Fig. 1(a), while the powder used in the evaporation is presented in Fig. 1(b). The analysis of Fig. 1(a) shows that the diffractograms present the typical diffuse profile of nanostructured materials. The four vertical blue lines stand for planes of SnO_2 crystals with rutile structure (JPCD 2003 file 01-088-0287). The sample annealed at 300 °C does not show any visible SnO_2 peak, although some peaks are present. These diffraction peaks have some correspondence with the (110) and (111) planes of SnO_2, which are located at $2\theta = 26.6°$ and 38.98°. The mismatches are +3% and -0.049% respectively. So, there is a possibility that the observed peaks are due to the film itself. Nevertheless, considering the large volume of the soda-lime glass used as substrate, and the fact that the thermal treatment used has a significant temperature as compared to the glass transition point of this substrate material (564 °C), there is possibility that these peaks can be due to a partial crystallization of the substrates. Checking for the diffraction peaks, we have found very good agreement of the observed peaks with the corresponding ones reported for magnesium silicate forstensite (Mg_2SiO_4, Match Software, entry 01-075-1448). The composition of forstensite is compatible with the soda-lime glass composition. This explanation is also consistent with the fact that the corresponding diffraction peaks are not observed when the film is treated at 1000 °C since in this case the substrate used is not soda-lime, but SiO_2. In the diffractogram of the sample annealed at 500 °C, it is possible to observe three SnO_2 small peaks, referring to the planes (110), (101) and (211) of rutile structure, even though the peaks for the possibly soda-lime glass substrate are still present. Several reports [2,9,11] found similar peaks on SnO_2 films deposited by RF magnetron sputtering. However, peaks corresponding to other sets of planes were found in these reports, such as (002), (112), (200) and (301), but with lower intensity. [2,10,11]. The method used here in the XRD measurement is the powder method (geometry 2θ-θ), so the peaks referring to planes (002), (112), (200) and (301) may be weaker and hidden by the substrate signal. For the diffractogram of the sample annealed at 1000 °C, these four peaks are clearly identified. They have higher definition and intensity when compared to the sample annealed at 500 °C. No peaks correlated to the rare earth doping Er^{3+} were found, probably due to its low concentration and dispersion in the films. It is possible to observe that the increase in the thermal annealing temperature has a strong influence on the crystallinity of the film. Ansari and coworkers [22] used tin oxide commercial analytical reagent as a precursor for evaporation on alumina substrate to evaporated SnO_2 and obtained diffraction patterns related to the material Sn_3O_4, which did not occur in the present case. The difference in the precursor may induce a different stoichiometry, leading to a different film crystallization and thus, to distinct X-Ray diffraction peaks.

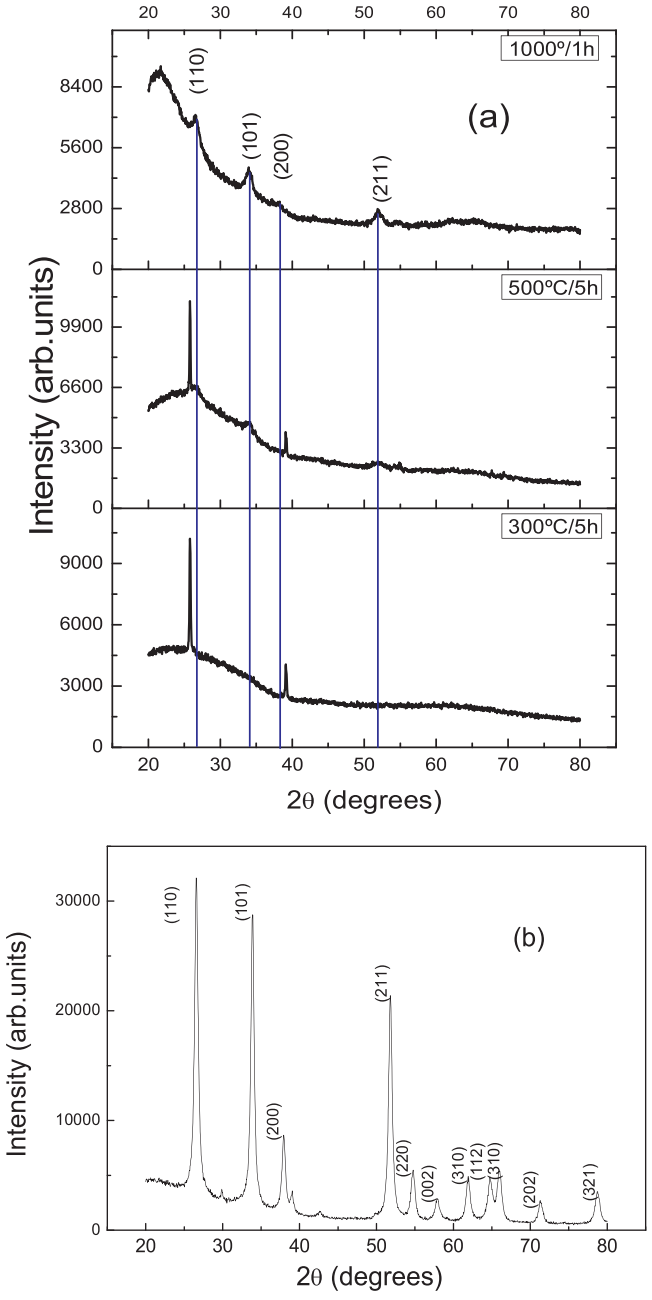

Fig. 1. (a) XRD for thin films - samples S1000, S500 and S300. (b) XRD of SnO_2:1at%Er^{3+} powder, obtained from sol-gel precursor solution, and used in the resistive evaporation.

Fig. 1(b) shows XRD of SnO_2 powder doped with 1at% Er^{3+} annealed at 1000 °C for five hours. The most intense peaks are identified, and are in agreement with the SnO_2 with tetragonal rutile structure (JPCD 2003 file 01-088-0287). It is important to mention that, similar to the thin films diffractograms (Fig. 1(a)), no peaks were observed regarding the erbium or any of its compounds in the powder matrix, probably due to the low concentration and dispersion in SnO_2 matrix.

Fig. 2 displays UV- near IR transmittance curves for SnO_2:1% Er^{3+} films annealed at 300 °C, 500 °C and 1000 °C. It shows that, except for the treatment at 500 °C, as the thermal annealing temperature increases, the film transmittance increases and the absorption edge shifts to higher energies. It has been observed that annealing processes above 600 °C (as in the case of sample S1000) improves the transmittance [11]. It is proposed that with increasing temperature, the Er^{3+} ions may disseminate into the film from interstitial sites to the substitutional

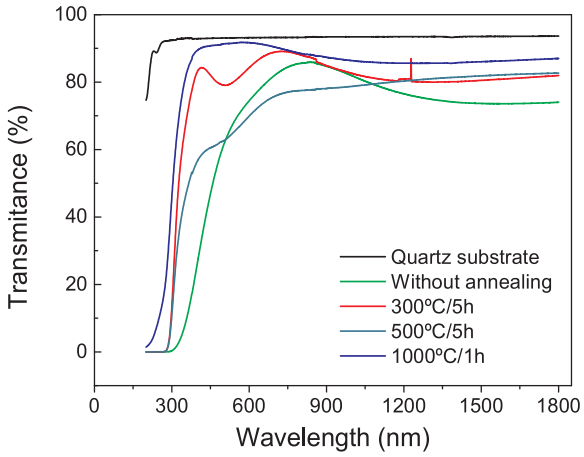

Fig. 2. Optical transmission spectra for SnO_2:Er films annealed at different temperatures.

positions, as reported for Zn diffusion in SnO_2 [11]. It is important to mention that the quartz substrate transmittance (Fig. 2) is well above the transmittance of the film treated at 1000 °C (S1000), assuring that although the thermal annealing temperature is high, the film remains on the substrate surface, even though the evaporation temperature of pure SnO_2 is lower [38].

The sample annealed at 500 °C is noticeably more opaque and exhibits high roughness, beginning to peel off the substrate, which justifies the lower transmittance. The shape of transmittance curve is similar to those reported for SnO_2 deposited on substrates heated to about 500 °C [39]. It is important to mention that the sample S500 shows higher electrical conductivity, as will be seen, also justifying the existence of donor-like defects in the sample [2,3,11,40], that may also influence on the transparency of the sample.

It is observed that transparency is in the 80–90% range in the visible region, which is in good agreement with the expected SnO_2 optical transmittance [2,10,11], since this material is used for transparent electrodes [1,3,14,18]. Sample S1000 which was submitted to the highest temperature of thermal treatment presents the highest transparency, and also has more evident XRD SnO_2 peaks, as seen in Fig. 1. This suggests better crystallinity. The interference fringes present for sample S300 allow for the evaluation of this film thickness [41], which is 240 nm.

The scanning electron microscopy (SEM) image of the surface for evaporated Er^{3+}-doped SnO_2 samples without annealing (as-grown) is shown in Fig. 3(a). The corresponding surface is rather smooth, with minor presence of visible grains or agglomerates. On the other hand, SEM images for the surface of SnO_2:1%Er^{3+} annealed at 1000 °C, is shown in Fig. 3 (b), and displays a high density of grains with sizes of about 1–3 μm, in good agreement with the report by Ansari and coworkers [22], that obtained films by the resistive evaporation technique with same dimensions particles. In our case, when tin oxide films were deposited by resistive evaporation on top of a GaAs substrate, particles acquire similar dimensions, but with greater particle spacing when compared to SnO_2 deposited by sol-gel-dip-coating on top of GaAs [42]. No evidence is found of clusters in Fig. 3(a), indicating good film uniformity.

Fig. 4(a) shows EDX for sample S1000 scanned all over the surface. In the left top figure, the image of the surface distribution of elements Sn, O and Er placed together is shown. In the other images, the individual distribution of each element is shown, for the analyzed area (O in green, Sn in red and Er in blue). Fig. 4(b) also shows EDX scanning, for the sample S300. Then, as in 4(a), the elements Sn, O and Er are placed together in the left top figure, and the individual concentrations of each element for the analyzed area (O in green, Sn in red and Er in blue) are shown separately.

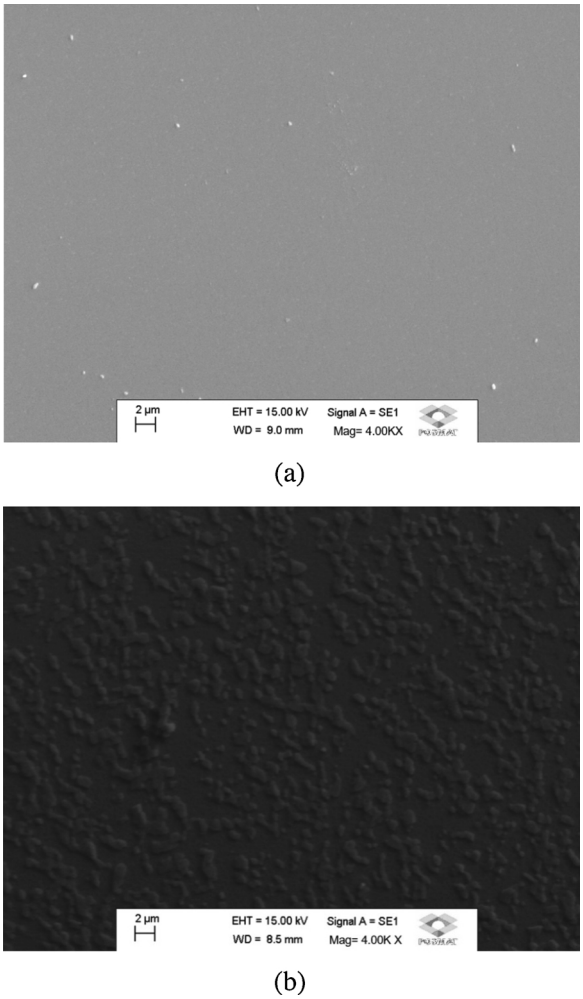

Fig. 3. Surface SEM of evaporated Er^{3+}-doped SnO_2 : (a) as-grown. (b) annealed at 1000 °C.

A uniform distribution of Sn (in red) and O (in green) elements are identified for both samples, S300 and S1000, indicating good homogeneity of the film and the quality of the combined deposition technique. However, in the case of the Er, EDX image of the S1000 sample, which was subjected to a high temperature of annealing, shows a higher Er ion dispersion (Fig. 4a), when compared to S300 sample, which was submitted to a lower temperature of annealing (Fig. 4b). Looking at the EDX image of the sample S1000 it appears that the erbium ions have disappeared from the region reached by the EDX analysis whereas the EDX image of sample S300 shows a much more uniform distribution. The higher annealing temperature increases the crystallite size, allowing the Er ions to populate more lattice sites, substitutional to Sn, instead of being located at grain boundaries. It apparently causes the dispersion of erbium ions into the sample, preventing a larger number of ions to be visualized in the EDX distribution image.

AFM micrographs for SnO_2 film deposited by resistive evaporation on GaAs substrate (GS1 sample) are shown in Fig. 5. On the left side, micrographs concern a 3D image and on the right side, the 2D surface image. The root mean square (rms) roughness for this film was 6.3 nm, which is very close to the values reported for films deposited by magnetron sputtering by Leng and coworkers [2]. The surface morphologies of film deposited by resistive evaporation are quite regular when compared to films deposited by dip coating (rms roughness of 10.3 nm) [1,28]. For the sample GS1, where the SnO_2 layer is deposited on GaAs, the average dimension of grains ranges from 100 to 150 nm, whereas samples deposited by dip-coating on glass substrates present dimensions of the grains with magnitude of 30–50 nm with no evidences of clusters [28]. The evaporation of the tin dioxide allowed for an increase in grain size when compared to the dip-coating method.

Values of roughness (rms) could be decreased using more sophisticated deposition techniques, such as PLD (0.6 nm) [16], CVD (1.81 to 0.259 nm) [13,16], CBD (2.55 to 1.3 nm) [1] or sputtering (0.26 nm) [25]. It is important to mention that by using a GaAs substrate, which has a completely different structure from SnO_2, it creates stresses at the substrate / film interface, which may influence the surface roughness.

3.2. Photoluminescence results

Figs. 6 and 7 show photoluminescence (PL) results for S1000, S500, S300 and GS2 samples (samples with different annealing temperatures and different substrates). A SEM top image of the junction GaAs/SnO_2, and the corresponding sample diagram are also shown in Fig. 7. As can be seen in the SEM image the surface is quite smooth, attesting to the good quality of the heterostructure.

In the PL measurements, excited using the line 325 nm of a He-Cd laser, it is possible to notice a broadband from 518.3 nm to 530.8 nm. However, this band is only observed for the sample treated at 300 °C for five hours (Fig. 6). In samples treated at 500 °C and 1000 °C, it was not possible to observe any type of emission. This PL broadband is different from the PL originated from SnO_2 matrix [43], which is blue shifted compared to the present result, assuring that the observed transition of Fig. 6 comes from the Er^{3+} ion. It may be result of the overlapped Er^{3+} transitions $^2H_{11/2}\rightarrow{}^4I_{15/2}$ and $^4S_{3/2}\rightarrow{}^4I_{15/2}$ respectively [19,26,30,35–37,44–46]. All of these references found similar broad bands for Er^{3+} emissions, even though they are more intense in some cases. Excitation with a diode laser (532 nm line) does not lead to any band in the photoluminescence spectra.

It is interesting to analyze Fig. 6 taking into account the EDX scanning measurements (Fig. 4). The image of S300 shows much more Er as compared to S1000. Then, when irradiating with the laser beam, a higher number of Er centers will be excited in S300, justifying its emission, and the absence of PL signal from the S1000.

Concerning Fig. 7, it can be observed that when there is a GaAs layer below the SnO_2 film (sample GS2) the spectrum is somewhat different, a emission is observed at 530.8 nm, which may be related to only one of the Er^{3+} transitions ($^4S_{3/2}\rightarrow{}^4I_{15/2}$), instead of the overlapped transitions, which is seen only for the lowest temperature. This specific emission is not observed for the other samples, suggesting that the GaAs layer directly influenced the Er emission. It is interesting to mention that rare earth emission in SnO_2 deposited on GaAs was previously observed [42], and the rare earth emission is more evident for lower temperature of annealing, that, unlike the present case, were associated with the existence of Eu agglomerates on the sample surface. In the present case, the GS2 sample, whose luminescence associated with the Er ions is shown in Fig. 7(a), was not annealed. We believe that the luminescence of GS2 sample may have similar reasons, i.e. related to a low (or none) annealing temperature, which leads to concentrated doping areas. We must recall that in the case of samples evaporated on glass substrate (Fig. 6), the lower temperature of annealing (S300) presented luminescence, in full accordance with this explanation.

The $^2H_{11/2}\rightarrow{}^4I_{15/2}$ emission has been reported and maybe observed when $^4S_{3/2}$ level is excited because the $^2H_{11/2}$ level is populated from the $^4S_{3/2}$ level via a fast thermal equilibrium between these two levels [27]. This observation is usually related with the up-conversion process in sol-gel materials [19], which does not occur in GS2 sample, unlike the G300 sample, where the $^2H_{11/2}\rightarrow{}^4I_{15/2}$ emission is observed only inside the broad band. The mechanism for emission originated from the $^4S_{3/2}\rightarrow{}^4I_{15/2}$ transitions is related with multiphonon relaxation [26]. On the other hand, the low concentration of Er^{3+} ions in SnO_2 nanocrystals are excited by non-radiative energy transfer from the semiconductor nanocrystalline host [35].

In the present case, the higher annealing temperature apparently

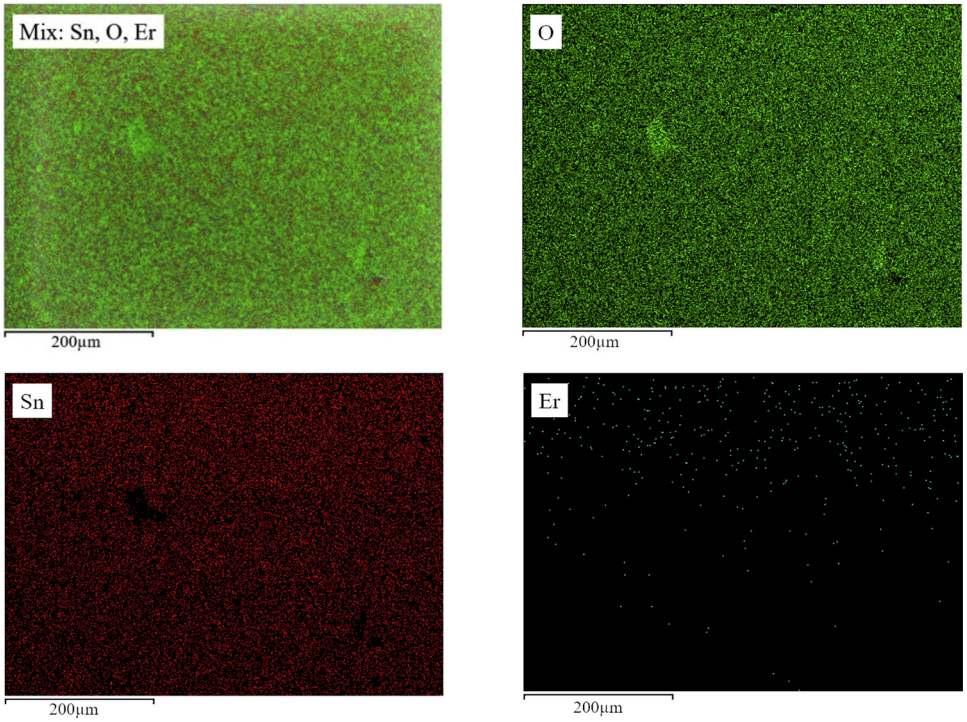

Fig. 4. Scanning EDX for evaporated Er-doped SnO_2 samples annealed at different temperatures.

causes the diffusion of erbium ions to substitutional Sn sites, leading to a much lower incidence of Er^{3+}-reach regions (at grain boundaries), making the observation in the EDX scanning image difficult (Fig. 4). As already has been mentioned, these results are different from Bueno and coworkers [42], in the case of Eu-doped samples, where the existence of rare-earth ion agglomerates on the top layer surface leads to emission from GaAs/SnO_2 heterostructures unlike SnO_2 films deposited on glass substrate, which do not show any emission until the thermal annealing temperature gets very high.

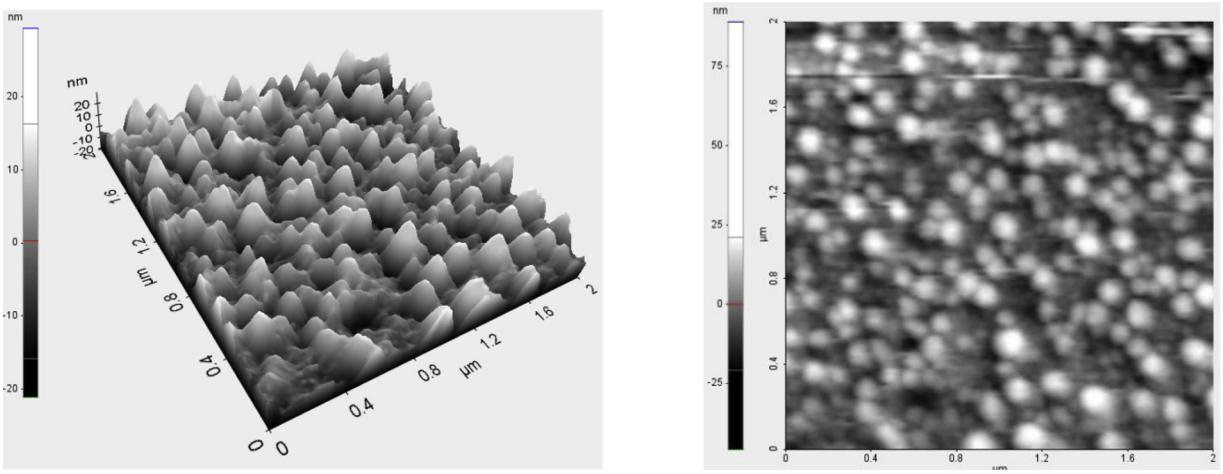

Fig. 5. Atomic Force Microscopy images in a 2 µm x 2 µm range for GS1 sample: (left) 3 D image, (right) 2D.

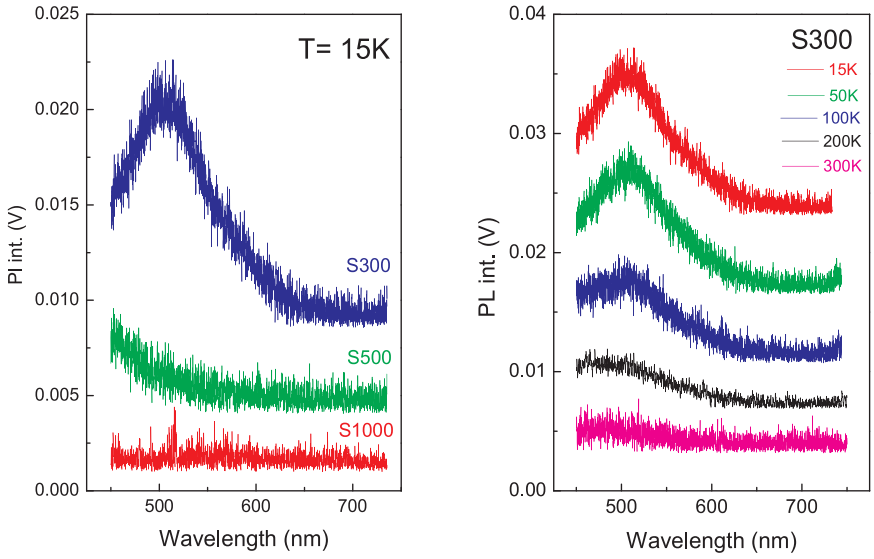

Fig. 6. Photoluminescence at 15 K, of evaporated Er-doped SnO_2 samples, annealed at different temperatures (left). Photoluminescence of sample S300, measured at different temperatures (right).

3.3. Electrical characterization

Concerning electrical measurements, Fig. 8 brings current versus voltage (IxV) profile for samples S300, S500 and S1000 performed at room temperature and pressure. In the inset of Fig. 8, the resistivity is presented as a function of annealing temperature, evaluated from the experimental data exhibit in the main figure. It can be seen that all the samples present ohmic behavior. Further, they also exhibit very stable signals in the measured voltage range, leading to precise reproducible data. It is possible to observe that the sample with higher annealing temperature (S1000) has a higher resistance, even though it presents higher intensity of the XRD peaks, related to SnO_2 rutile phase (Fig. 1), which suggests better crystallinity, and greater transparency (Fig. 2). The observed effect is the decrease in the current for S1000 sample using the same applied bias, in other words, a smaller slope in the IxV curve. This is consistent with previous report, on thermal annealing under vacuum conditions [29], which leads to higher conductivity. In the present case, considering the thermal annealing under room atmosphere conditions, it is expected that the higher temperature leads to higher amount of adsorbed oxygen species, increasing the resistivity. Another hypothesis is that at temperatures close to 1000 °C, oxygen atoms break the bonds in SnO_2 [47], and the effect is an increase in the resistivity of the material. On the other hand, the EDX results (Fig. 4) show that Er^{+3} ions diffuses into the sample, and considering the acceptor nature of this trivalent rare-earth ion, mainly when located at subtitutional Sn^{4+} sites, it induces more charge compensation with the free electrons in the SnO_2 matrix, contributing to the higher resistivity of sample S1000. The sample annealed at 500 °C is the most conductive, whereas the sample treated at 300 °C has intermediate resistivity. However, sample S300 presented the most intense PL (Fig. 5), which, as already discussed is related to the presence of Er^{3+} ions located at grain boundaries (Fig. 4). Thus, it is expected that this sample is less resistive than S1000 one, because the charge compensation with free electrons is more efficient for substitutional Er^{3+} ions than for grain boundaries located ions. On the other hand, for sample S500, annealed at 500 °C, the effect of larger crystallites is dominant in this case, because larger grains (induced by higher temperature) lead to a lower grain boundary scattering in this sample when compared to S300, yielding a higher conductivity.

Fig. 9 shows current-voltage measurements for the samples S300 and S1000 carried out in the dark and under the effect of irradiation with different light sources: 1) He-Ne laser (628 nm) and 2)InGaN LEDs (440–460 nm). The inset on the right side also shows the effect of irradiation with He-Cd laser (325 nm). Both samples present an ohmic behavior in the dark and under optical excitation. Excitation with the He-Ne laser leads to practically the same behavior, since this light

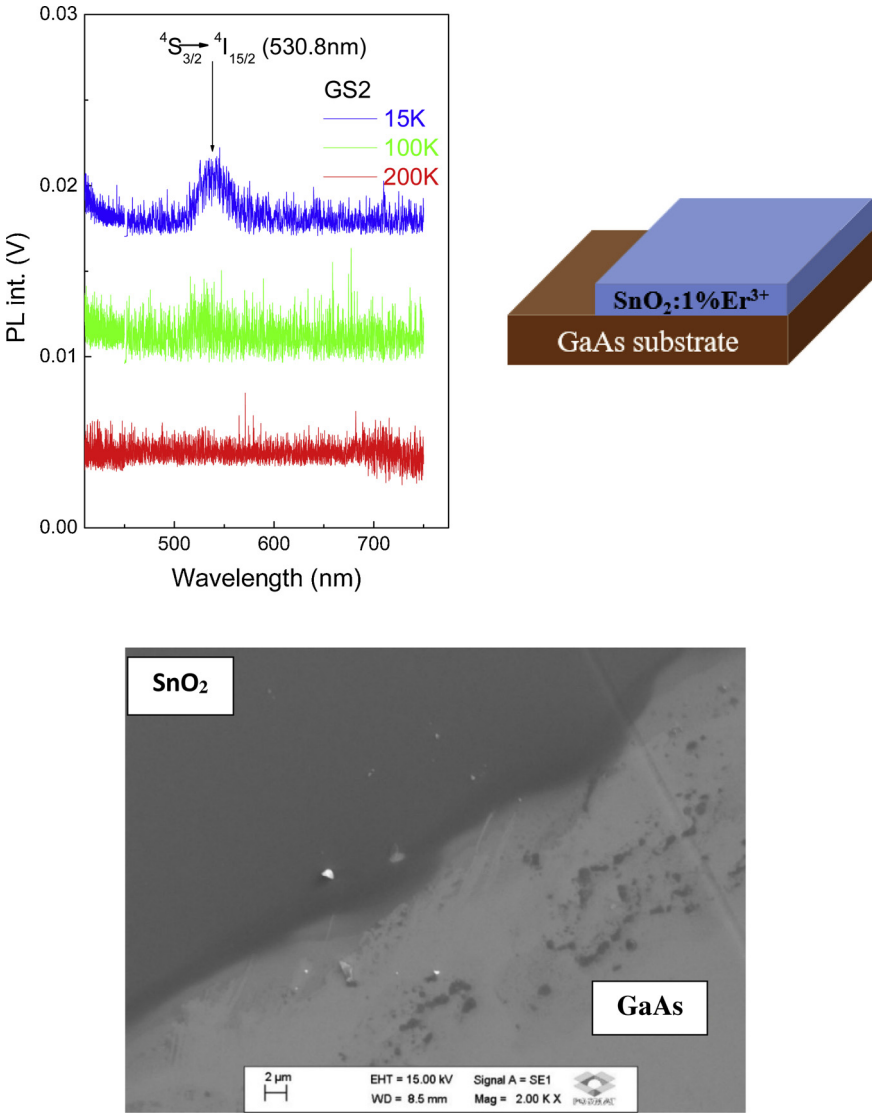

Fig. 7. (top) PL for Er-doped evaporated SnO_2 samples grown on top of GaAs (GS2) and sample geometry diagram. (bottom) SEM surface image, showing both film regions.

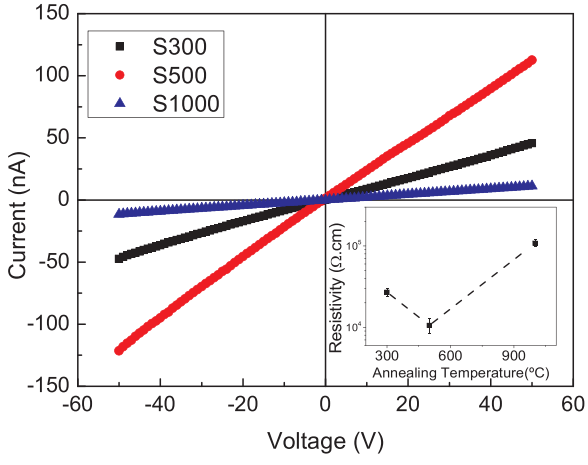

Fig. 8. Current as function of voltage for evaporated Er-doped SnO_2 samples, annealed at different temperatures. Inset: resistivity versus annealing temperature. Line is drawn just as a guide to the eyes.

source has energy (1.97 eV) somewhat lower than the tin oxide bandgap, and thus does not cause significant change in the conduction of the samples. On the other hand, when excited with the InGaN LED (2.75 eV), the sample S300 was poorly stimulated (Fig. 4a), however, sample S1000 (Fig. 4b) exhibits a significant increase in the current. Such excitation was permanent, since the sample remained in this state for days. In the sample S1000, Er^{3+} ions are mainly substitutional, as already discussed, justifying the higher resistivity of this material. When excited with the LED, the excitation energy (average 2.75 V) is close to the excitation energy of transitions from level $^4I_{15/2}$ to levels $^4F_{5/2}$ (2.74 eV) and $^4F_{3/2}$ (2.79 eV) [19] that suggests that this light source may excite ions in the S1000 sample more efficiently. Then, sample S1000 which is the most resistive in the dark, due to acceptor Er^{3+} ions, becomes the most conductive under light effect. Considering that the excitation of Er^{3+} ion promotes electron transfer to the SnO_2 conduction band, they remain in a conductive state for a long time, without decaying to the Er^{3+} ground state, justifying the permanent effect on the conductivity. The effect of excitation of SnO_2 layers with distinct light sources for the electrical properties has been explored before [29], and it has also been reported a significant difference in the decay of photo-excited conductivity [48] when the sample is undoped or doped with Er^{3+} ions, the former present related centers with

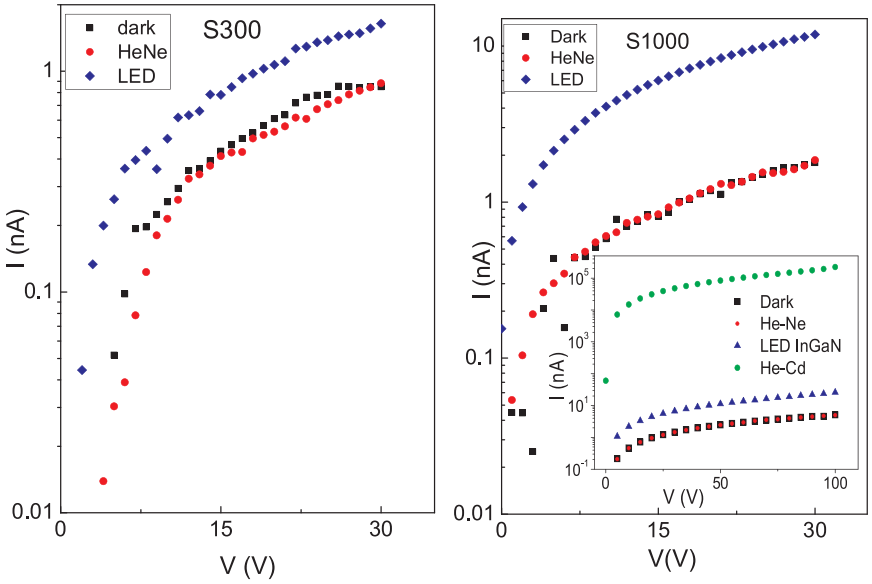

Fig. 9. Current as function of voltage at room temperature, for sample S300 (left) and S1000 (right) in the dark, and under effect of He-Ne laser (628 nm) and InGaN LED (440–460 nm). Inset: same data for sample S1000, also showing excitation with He-Cd laser (325 nm).

thermally activated capture cross section. The decay of photo-excited conductivity is temperature and Er-concentration dependent. The capture barrier (E_{cap}) has different values whether the defect is substitutional to Sn^{4+} site or located at grain boundaries, being lower for substitutional sites. A lower E_{cap} also means an easier photo excitation to the conductive state, since the localization presents less electron-phonon coupling for the substitutional site (S1000) than for the asymmetric boundary layer sites (sample S300), justifying the higher conductivity of the S1000 sample, after InGaN LED excitation. In the inset of Fig. 9, it is possible to observe that excitation with the He-Cd laser, the same used for PL excitation (Figs. 6 and 7) leads to a much higher conductivity, associated with excitation of electron-hole pairs. This effect is similar to the observed for Eu-doped GaAs/SnO_2 heterostructures, where the excitation were much more efficient when the SnO_2 is the top layer, whereas the GaAs acts as a shield layer when deposited on top of the heterostructure [49,50].

4. Conclusion

The combination of sol-gel and resistive evaporation techniques in a new route to obtain Er-doped tin dioxide thin films on different types of substrates produced effective results. EDX mapping confirmed that the Er is uniformly dispersed on the films. It was observed that the optical and electrical properties, as well as the Er distribution are highly dependent on the thermal annealing temperature.

PL measurements show that the annealing temperature influences the Er^{3+} emission: sample deposited on glass substrate and annealed at 300 °C shows a broad PL band due to overlap of emissions from Er^{3+} transitions $^2H_{11/2}\rightarrow{}^4I_{15/2}$ and $^4S_{3/2}\rightarrow{}^4I_{15/2}$, whereas the sample annealed at 1000 °C does not show any emission. This luminescence band (and the absence of it) is related to the Er^{3+} concentration on the different crystalline sites, as revealed by scanning EDX of the tin dioxide surface. However, the luminescence seems to come from Er agglomerates, which are more visible in the EDX mapping at lower annealing temperature. When GaAs is used as substrate, only the emission related to $^4S_{3/2}\rightarrow{}^4I_{15/2}$ transition is observed.

The diffusion of Er ions towards substitutional sites, provided by a higher thermal annealing temperature, also causes higher electron trapping, inducing lower conductivity for the higher annealing temperature sample, increasing the recombination with free electrons from the matrix. On the other hand, these trapped electrons are more efficiently excited when compared to surface located ions.

Evaporated SnO_2 films have a more stable electrical signal when compared to films deposited by sol-gel-dip-coating and provide some advantages, such as deposition on hydrophobic surfaces, and the possibility of utilization of shadow masks. These properties are important in order to achieve the desired structure pattern, and contribute to the design and construction of more efficient optoelectronic devices.

Acknowledgements

We would like to thank financial support from CAPES, CNPq, and FAPESP (grants 2016/12216-6 and 2017/18916-2).

Appendix A. Supplementary data

Supplementary material related to this article can be found, in the online version, at doi:https://doi.org/10.1016/j.materresbull.2019.110585.

References

[1] S.M. Al-Jawad, A.K. Elttayf, A.S. Saber, Influence Of Annealing Temperature On The Characteristics Of Nanocrystalline SnO_2 Thin Films Produced By Sol–Gel And Chemical Bath Deposition For Gas Sensor Applications, Surf. Rev. Lett. 24 (2017) 1–13 1750104.
[2] D. Leng, L. Wu, H. Jiang, Y. Xhao, J. Zhang, W. Li, L. Feng, Preparation and properties of SnO_2 film deposited by magnetron sputtering, Int. J. Photoenergy 2012 (2012) 1–6.
[3] R. Rai, Study of structural and electrical properties of pure and Zn-Cu doped SnO2, Adv. Mater. Lett. 1 (2010) 55–58.
[4] S. Das, V. Jayaraman, SnO_2: a comprehensive review on structures and gas sensors, Prog. Mater. Sci. 66 (2014) 112–255.
[5] L.P. Ravaro, L.V.A. Scalvi, Influence of pH of colloidal suspension on the electrical conductivity of SnO_2 thin films deposited via Sol-Gel-Dip-Coating, Mater. Res. 14 (2011) 113–117.
[6] A.S.M.S. Rahman, M.H. Islam, C.A. Hogarth, AC electrical properties of vacuum-evaporated SiO/SnO_2 films, Int. J. Electron. 62 (1987) 167–179.
[7] D.H.O. Machado, L.V.A. Scalvi, C.F. Bueno, Photoluminescence of Rare-Earth Ions in the Nanocrystalline GaAs/SnO2 Heterostructure and the Photoinduced Electrical Properties Related to the Interface, Condens. Matter. 2 (2017) 1–10.
[8] K. Tadanaga, T. Fujii, A. Matsuda, T. Minami, M. Tatsumisago, Micropatterning of sol-gel derived thin films using hydrophobic-hydrophilic patterned surface, J. Solgel Sci. Technol. 31 (2004) 299–302.
[9] T. Gui, L. Hal, W. Wang, L. Yuan, W. Jia, X. Dong, Structure and features of SnO_2 thin films prepared by RF reactive sputtering, Chin. Opt. Lett. 8 (2010) 134–136.
[10] S.U. Lee, J.H. Boo, B. Hong, Structural, electrical, and optical properties of SnO_2: Sb films prepared on flexible substrate at room temperature, J. Appl. Phys. 50 (2011)

01AB10.
[11] J.M. Ni, X.J. Zhao, J. Zhao, Electrical and Optical Properties of p-Type Transparent Conducting SnO_2:Zn Film, J. Inorg. Organomet. Polym. Mater. 22 (2012) 21–26.
[12] R.A. Casali, J. Lasave, M.A. Caravara, S. Koval, C.A. Ponce, R.L. Migoni, Ab initio and shell model studies of structural, thermoelastic and vibrational properties of SnO_2 under pressure, J. Phys. Condens. Matter 25 (2013) 135404.
[13] O.A. Hussein, N.A. Ali, Effect of capillary tube on structural and optical properties of SnO_2 thin films prepared by APCVD, International J. Chem. Tech. Research 10 (2017) 202–207.
[14] F.H. Alshammari, M.K. Hota, K. Hota, Z. Wang, Atomic-layer-Deposited SnO_2 as gate electrode for indium-free transparent electronics, Adv. Electron. Mater. 3 (2017) 1–9 1700155.
[15] X. Wang, N. Arronyadet, Y. Zhang, M. Mecklenburg, X. Fang, H. Chen, E. Goo, C. Zhou, Aligned epitaxial SnO_2 nanowires on sapphire: Growth and device applications, Nano Lett. 14 (2014) 3014–3022.
[16] H. Kim, R.C.Y. Auyeung, A. Piqué, Transparent conducting F-doped SnO_2 thin films grown by pulsed laser deposition, Thin Solid Films 516 (2008) 5052–5056.
[17] Y. Liu, Y. Jiao, Z. Zhang, F. Qu, A. Umar, X. Wu, Hierarchical SnO_2 nanostructures made of intermingled ultrathin nanosheets for environmental remediation, smart gas sensor, and supercapacitor applications, ACS Appl. Mater. Interfaces 6 (2014) 2174–2184.
[18] M. Gharesi, M. Moalaghi, N. Dehghani, M. Ansari, Field-assisted diffusion of silver in SnO_2 thin films, J. Phys. Conf. Ser. 939 (2017) 012007.
[19] C. Bouzidi, A. Moadhen, H. Elhouichet, M. Oueslati, Er^{3+}-doped sol-gel SnO_2 for optical laser and amplifier applications, Appl. Phys. B Lasers Opt. 90 (2008) 465–469.
[20] H. Wang, A.L. Rogach, Hierarchical SnO_2 nanostructures: recent advances in design, synthesis, and applications, Chem. Mater. 26 (2014) 123–133.
[21] V. Bonu, A. Das, A.K. Sivadasan, A.K. Tyagi, S. Dhara, Invoking forbidden modes in SnO_2 nanoparticles using tip enhanced Raman spectroscopy, J. Raman Spectrosc. 46 (2015) 1037–1049.
[22] S.G. Ansari, S.W. Gosavi, S.A. Gangal, R.N. Karekar, R.C. Aiyer, Characterization of SnO_2-based H_2 gas sensors fabricated by different deposition techniques, J. Mater. Scie.: Mater. Electr. 8 (1997) 23–27.
[23] X. Li, T. Peng, Y. Zhang, Y. Wen, Z. Nan, A new efficient visible-light photocatalyst made of SnO_2 and cyclized polyacrylonitrile, Mat. Res. Bull. 97 (2018) 517–522.
[24] D. Wei, Z. Xu, J. Liang, X. Li, Y. Qian, Rational design of SnO_2 aggregation nanostructure with uniform pores and its supercapacitor application, J. Mater. Sci.: Mater. Electron. 26 (2015) 6143–6147.
[25] L. Skowronski, R. Szczesny, K. Zdunek, Optical and microstructural characterization of amorphous-like Al_2O_3, $SnO_2$and TiO_2 thin layers deposited using a pulse gas injection magnetron sputtering technique, Thin Solid Films 632 (2017) 112–118.
[26] A. Moadhen, C. Bouzidi, H. Elhouichet, R. Chtourou, M. Oueslati, Concentration and temperature dependence of visible up-conversion luminescence in sol-gel SnO2doped with erbium, Opt. Mater. (Amst) 31 (2009) 1224–1227.
[27] E.J. Nassar, K.J. Ciuffi, R.R. Gonçalves, Y. Messaddeq, S.J.L. Ribeiro, Filmes de titânio-silício preparados por spin e dip-coating, Quim. Nova 23 (2003) 674–677.
[28] E.A. Morais, L.V.A. Scalvi, L.P. Ravaro, M.S. Li, E.A. Floriano, Optical and transport properties of rare-earth trivalent ions located at different sites in sol-gel SnO2, J. Phys. Conf. Ser. 249 (2010) 012005.
[29] F.R. Messias, B.A.V. Vega, L.V.A. Scalvi, M. Siu Li, C.V. Santilli, S.H. Pulcinelli, Electron scattering and effects of sources of light on photoconductivity of SnO_2 coatings prepared by sol-gel, J. Non-Crystalline Solids 247 (1999) 171–175.
[30] N.J. Shivaramu, B.N. Lakshminarasappa, K.R. Nagabhushana, H.C. Swart, F. Singh, Photoluminescence, thermoluminescence glow curve and emission characteristics of Y_2O_3:Er^{3+} nanophosphor, Spectrochim Acta - Part A Mol. Biomol. Spectrosc. 189 (2018) 349–356.
[31] S. Coffa, G. Franzò, F. Priolo, R. Serna, Temperature dependence and quenching processes of the intra-4f luminescence of Er in crystalline Si, Phys. Rev. B 49 (1994) 16313–16320.
[32] E.A. Morais, L.V.A. Scalvi, M.R. Martins, S.J.L. Ribeiro, Analysis of Er^{3+} incorporation in SnO_2 by optical investigation, Braz. J. Phys. 36 (2006) 270–273.
[33] J. Castaneda-Contreras, M.A. Meneses-Nava, O. Barbosa-Garcia, R.A. Rodriguez-Rojas, M.V. Félix, Opt. Mater. 29 (2006) 38–42.
[34] T.T.T. Van, S. Turrel, B. Capoen, L. Van Hieu, M. Ferrari, D. Ristic, L. Boussekey, C. Kinowski, Environment segregation of Er^{3+} emission in bulk sol-gel-derived SiO_2-SnO_2 glass ceramics, J. Mater. Sci. 40 (2014) 8226–8233.
[35] J. Del-Castillo, V.D. Rodrıguez, A.C. Yanes, J. Mendez-Ramos, Energy transfer from the host to Er^{3+} dopants in semiconductor SnO_2 nanocrystals segregated in sol-gel silica glasses, J. Nanopart. Res. 10 (2008) 499–506.
[36] J. Yang, L. Zhang, L. Wen, S. Dai, L. Hu, Z. Jiang, Optical transitions and upconversion luminescence of Er^{3+}/Yb^{3+}-codoped halide modified tellurite glasses, J. Appl. Phys. 95 (2004) 3020–3026.
[37] H. Lin, G. Meredith, S. Jiang, X. Peng, T. Luo, N. Peyghambarian, E.Y.B. Pun, Optical transitions and visible upconversion in $Er3^{+}$ doped niobic tellurite glass, J. Appl. Phys. 93 (2003) 186–191.
[38] H.W. Ra, K.J. Kim, Y.H. Im, Multiple branch growth of SnO2 nanowires by thermal evaporation process, Superlattice Microst. 44 (2008) 728–734.
[39] V. Vasu, A. Subrahmanyam, Electrical and optical properties of pyrolytically sprayed SnO_2 film—Dependence on substrate temperature and substrate-nozzle distance, Thin Solid Films 189 (1990) 217–225.
[40] S.E.K. Kim, M. Oliver, Structural, electrical, and optical properties of reactively sputtered SnO_2 thin films, Met. Mater. Int. 16 (2010) 441–446.
[41] J.L. Cisneros, Optical characterization of dielectric and semiconductor thin films by use of transmission data, Appl. Opt. 37 (1998) 5262–5270.
[42] C.F. Bueno, L.V.A. Scalvi, M.S. Li, M.J. Saeki, Luminescence of Eu^{3+} in the thin film heterojunction GaAs/SnO_2, Opt. Mater. Express 5 (2015) 59–72.
[43] J. Mazloom, F.E. Ghodsi, Spectroscopic, microscopic, and electrical characterization of nanostructured SnO_2:Co thin films prepared by sol–gel spin coating technique, Mater. Res. Bull. 48 (2013) 1468–1476.
[44] Y. Fu, Y. Shi, M. Xing, Y. Tian, X. Luo, Up-conversion luminescence properties of $NaYTiO_4$: Yb^{3+}, Er^{3+} under 1550 and 980 nm excitations, J. Mater. Sci. 52 (2017) 408–414.
[45] P. Kostka, I. Kabalci, T. Tay, P. Gladkov, J. Zavadil, Investigation of Er doped zinc borate glasses by low-temperature photoluminescence, J. Lumin. 192 (2017) 1104–1109.
[46] J. Lei, B. Liu, Q. Min, L. Zhao, D. Zhou, J. Qiu, X. Xu, X. Yu, Simultaneous phase and morphology control of Ba_2YbF_7: Er^{3+} upconversion nanocrystals through La^{3+} doping, Mater. Res. Bull. 115 (2019) 242–246.
[47] R.H. Lamoreaux, D.L. Hildenbrand, L. Brewer, High-Temperature Vaporization Behavior of Oxides II. Oxides of Be, Mg, Ca, Sr, Ba, B, Al, Ga, In, Tl, Si, Ge, Sn, Pb, Zn, Cd, and Hg, J. Phys. Chem. Ref. Data 16 (1987) 419–443.
[48] E.A. Morais, L.V.A. Scalvi, Electron trapping of laser-induced carriers in Er-doped SnO_2 thin films, J. European Ceramic Society 27 (2007) 3803–3806.
[49] T.F. Pineiz, L.V.A. Scalvi, M.J. Saeki, E.A. Morais, Interface formation and electrical transport in SnO_2:Eu^{3+}/GaAs heterojunction deposited by sol–gel dip-coating and resistive evaporation, J. Electron Mater. 39 (2010) 1170–1176.
[50] T.F. Pineiz, E.A. Morais, L.V.A. Scalvi, C.F. Bueno, Interface formation of nanostructured heterojunction SnO_2:Eu/GaAs and electronic transport properties, Appl. Surf. Science 267 (2013) 200–205.